Accepted Manuscript

Graphene oxides as nanofillers in polysulfone ultrafiltration membranes: Shape matters

Yi Jiang, Qingqing Zeng, Pratim Biswas, John D. Fortner

PII: S0376-7388(18)32445-1

DOI: https://doi.org/10.1016/j.memsci.2019.03.056

Reference: MEMSCI 16957

To appear in: *Journal of Membrane Science*

Received Date: 6 September 2018

Revised Date: 25 January 2019

Accepted Date: 18 March 2019

Please cite this article as: Y. Jiang, Q. Zeng, P. Biswas, J.D. Fortner, Graphene oxides as nanofillers in polysulfone ultrafiltration membranes: Shape matters, *Journal of Membrane Science* (2019), doi: https://doi.org/10.1016/j.memsci.2019.03.056.

Graphene Oxides as Nanofillers in Polysulfone Ultrafiltration Membranes: Shape Matters

Yi Jiang[1,2]*, Qingqing Zeng[2], Pratim Biswas[2], John D. Fortner[2,3]*

[1]Department of Civil and Environmental Engineering, the Hong Kong Polytechnic University, Kowloon, Hong Kong, China

[2]Department of Energy, Environmental, and Chemical Engineering, Washington University in St. Louis, St. Louis, MO 63130, United States

[3]Department of Chemical and Environmental Engineering, Yale University, New Haven, CT 06520, United States

Re-Submitted to

Journal of Membrane Science

January, 2019

*To whom correspondence should be addressed:

Yi Jiang: Tel: +852-2766-6044; Fax: +852-2334-6389; Email: yi-cee.jiang@polyu.edu.hk

John D. Fortner: Tel: +1-314-935-9293; Fax: +1-314-935-5464; Email: john.fortner@yale.edu

Abstract

While a number of graphene oxide (GO) materials have been evaluated as nanofillers in ultrafiltration membranes, there remain outstanding questions regarding GO material properties relating to membrane structure(s) and eventual performance (i.e. structure-performance relationships). In this work, we synthesize, apply, and evaluate GO analog materials of different shape, flat GO and crumpled GO (CGO), as nanoscale fillers in polysulfone (PSF) ultrafiltration membranes. GO/CGO-PSF composite membranes were synthesized via phase inversion, characterized using both microscopic and spectroscopic techniques, and compared with respect to permeability, rejection, and anti-fouling properties. Experimental results show that graphene shape alone results in varied performance. Observed differences are attributed to the (more) effective dispersion/stability of CGO nanoparticles in solvent (NMP) as a result of shape effects, which lowers the tipping mass percentage after which the effect of viscosity increase outweighs that of hydrophilicity increase. Our results also suggest that the change(s) in membrane porosity is likely to be a more important factor compared to surface hydrophilicity in determining ultrafiltration membrane performance when graphene oxides are applied with these mass percentages. In addition to the effect of GO shape, this study also highlights the importance of nanoparticle dispersiblity/stability in organic solvents when constructing the process-structure-performance relationships for nano-enabled ultrafiltration membranes synthesized via phase inversion.

Keywords: Graphene oxide, shape, dispersibilitiy, viscosity, porosity, hydrophilicity

1. Introduction

Recent advances in materials science and nanoscale engineering have offered opportunities to develop advanced water treatment technologies. In particular, surface nano-engineering of conventional polymeric membranes has shown tremendous potential [1]. To make nano-enabled membranes, functional nanomaterials are commonly surface-coated onto, or impregnated into, conventional polymeric matrices (i.e., as nanofillers). Nanofiller materials have attracted attention due to the ease with which they can be readily integrated into current state-of-art technologies for membrane fabrication, including phase inversion and interfacial polymerization. To date, a number of nanoparticles have been incorporated, including oxides (e.g., TiO_2 [2, 3], Fe_3O_4 [4], SiO_2 [5, 6]), metals (e.g., Ag [7, 8], Cu [9]), carbon nanomaterials (e.g., C_{60} [10], carbon nanotube (CNT) [11, 12], graphene [13-16]), metal-organic frameworks (MOFs) [17, 18], and composites [19-21]. These studies have demonstrated membrane structural improvement with regard to surface hydrophilicity/charge, porosity, and mechanical stability. Corresponding enhancement in permeability, rejection, and anti-fouling properties were also observed [22].

Among the aforementioned nanomaterials, graphene-based nanofillers, including graphene oxide (GO), have attracted extensive research interest. In principle, GO partially remains as a one-atom-thick planar sheet with a sp^2-bonded carbon structure while being derivatized with oxygen functional groups both on the basal plane (typically as hydroxyl and epoxy groups) and at the sheet edges (as carboxyl and carbonyl based functionalities). For membrane applications, GO has some unique material advantages compared to graphene and other nanocarbon analogs. For example, its manufacturing consumes only ca. 1% of the energy needed for CNTs (i.e., 500-1000 MJ/Kg of GO vs. 100,000 MJ/Kg of CNTs) [23]. Further, it is highly tunable regarding both size and surface chemistry – the breadth of which can vary by

orders of magnitude [24, 25]. In addition, GO materials can be engineered to have different shapes and as hybrid/composite structures [26-28].

GO nanofillers have been primarily demonstrated in polymeric ultrafiltration (UF) membranes (e.g.,polysulfone (PSF), polyethersulfone (PES), and polyvinylidene difluoride (PVDF) [29]) via phase inversion synthesis routes. Relatively small amounts of GO (usually 0.1-6 wt.% with respect to the polymer) have been incorporated into conventional polymeric structures, including PSF [14, 30], PES [31], and PVDF [12]. Through these processes, membrane surface hydrophilicity increases due to migration of GO to the membrane surface, as a consistent decrease of ca. 20° (average) water contacting angle has been observed. Further, for most studies, overall membrane porosity also increases [30-32]. Both factors have been implicated in the increase of membrane permeability, which ranges from 10% to ×20 times compared to controls. However, the (relative) importance/contribution of surface hydrophilicity and structural porosity, as they relate to enhanced water flux and varied rejection performance, is still under debate [3, 31-33]. While simultaneous increase in both water permeability and rejection rate has been observed [12, 30, 31, 33, 34], inverse relationships between water permeability and rejection rate (e.g., the water permeability increased however the rejection decreased, and vice versa) have also been reported [20, 32, 35]. The relationship between water permeability and rejection performance is complicated by varied properties of the applied GO materials (surface functional groups, hybrids), different mass loadings, and tested filtrates (e.g., size and charge). For example, GO property variations are likely to have a significant impact on its aggregation/dispersion states in processing solvents such as NMP and DMF that are commonly used in membrane synthesis [36]. More evidence is thus needed for a complete mechanistic understanding of the role of GO properties in affecting/changing the membrane

structure(s) and ultimately membrane performance.

In this work, we aim to discern the role of GO shape as it affects PSF membrane structure and performance. 3D GO analog materials, termed as crumpled graphene oxide (CGO), were synthesized by physically crumpling flat GO nanosheets using evaporation-induced confinement force, while maintaining its surface chemistry (i.e. that of flat GO) [26]. The two synthesized materials (GO and CGO) were incorporated into PSF UF membranes at varied material loadings (0, 0.5, and 1.5 wt.%) via a well-established phase inversion synthesis route [12]. Pristine and composite membranes were characterized using microscopic and spectroscopic techniques, and compared in terms of water flux, rejection, and anti-fouling properties. Taken together, data presented provides new insights on how GO properties, such as shape, affect the membrane structures (surface hydrophilicity, porosity) and subsequent membrane performance.

2. Experimental

2.1 Synthesis and Characterization of Flat and Crumpled Graphene Oxides

Material Synthesis. GO was synthesized by oxidation and subsequent exfoliation of graphite, namely the modified Hummer's method [37], as described in detail in our previous work [26]. Briefly, 50 ml of concentrated sulfuric acid (H_2SO_4) was added into a beaker containing 2 g of graphite powders (45 µm, Sigma-Aldrich) at room temperature. The mixture was cooled to 0 °C by using an ice bath, and 6 g potassium permanganate ($KMnO_4$) was then slowly added while allowing it to warm to room temperature. The suspension was stirred for 2 h at 35°C before being cooled in an ice bath and diluted by 350 ml of deionized (DI) water. Then, hydrogen peroxide aqueous solution (H_2O_2, 30%) was added drop wise until the gas evolution ceased in order to reduce the residual permanganate. The suspension was then filtered, thoroughly washed

by DI water, and dried at room temperature for 24 h to obtain brownish graphite oxide powder. The dry graphite oxide powder was redispersed in DI water and sonicated for 2 h to get exfoliated nanosheets. The suspension was then centrifuged at 10,000 rpm for 30 min and the supernatant was used as the precursor for crumpled graphene oxide preparation by a furnace aerosol reactor (FuAR) method [26, 36].

In the aerosol-assisted process, flat GO sheets are crumpled in a water droplet under the capillary compression induced by rapid water evaporation. GO aqueous solution (~ 50 mg/L, mass concentration) was sprayed into micrometer-sized (2-4 μm) water droplets using a six-jet Collison nebulizer (BGI Incorporated) under a pressure of 14 psi, and the droplets were delivered by nitrogen gas into an alumina furnace reactor maintained at 200 °C to heat it for a few seconds. Each aerosolized droplet acts as a micro-reactor, in which flat GO sheets are crumpled under the capillary compression induced by rapid water evaporation. A furnace temperature of 200 °C was selected to achieve effective crumpling but maintain the surface chemistry, based on our previous studies [36]. The CGO nanoparticles were finally collected using a membrane filter (Millipore) at the end stream of the reactor, weighed and applied in the fabrication of PSF membranes as described later.

Material Characterization. Detailed material characterization methods were described in our earlier work [36]. The morphology and size of the GO/CGO samples were examined by transmission electron microscopy (TEM, TecnaiTM Spirit, FEI Co.) and atomic force microscopy (AFM, Veeco Nanoman). The sizes of GO/CGO were determined as the longest lateral dimension of a GO/CGO particle imaged by AFM or TEM and approximately 150 particles were counted for each material using ImageJ software. Surface chemistry information was obtained with X-ray photoelectron spectroscopy (XPS, PHI 5000 VersaProbe II equipped

with monochromatic Al Kα (1486.6 eV) X-ray source). ζ-potential (in 40 mg/L aqueous solution) was measured with a ZetaSizer Nano ZS instrument (Malvern Instruments, Worcestershire).

2.2 Membrane Fabrication

GO/CGO-PSF composite membranes were fabricated by the phase inversion method [14, 38] (Figure 1). A typical casting solution consists of 8.1 g of 1-Methyl-2pyrrolidinone (NMP, Sigma-Aldrich), 0.1 g of polyvinylpyrrolidone (PVP, Mw 10,000, Sigma-Aldrich), 1.8 g of PSF (beads, average Mn ~22,000, Sigma-Aldrich), and a desired amount of GO/CGO (0-1.5 wt. % to the PSF mass). First, the dispersion of GO/CGO in NMP was prepared. To make GO-PSF membranes, the graphite oxide power (0 - 27 mg, as described in Section 2.1) was directly added in the NMP solution (8.1 g) and sonicated for 1 h in order to obtain exfoliated GO and a homogeneous mixture. While for CGO-PSF membranes, the CGO particles were directly added into the NMP solution by washing off from the collection filter using NMP solution. A mild sonication was applied afterwards for further dispersion. The GO/CGO dispersion was then added with PVP (0.1 g) and PSF beads (1.8 g). The mixture was placed on a heating plate (60 °C) and stirred for 24 h, during which the PSF dissolved, forming a homogeneous casting solution. After 24 h, the casting solution was cooled to room temperature slowly in order to remove any bubbles.

Membrane casting was performed using a casting knife (EQ-Se-KTQ-150D, MTI Corp.) on a clean glass plate with a denominated thickness of 200 μm. Immediately after casting, the thin film was immersed into a water bath to initiate phase inversion. During the process, the casting solution was transformed into a two phase system, namely, a solid polymer-rich phase that formed the membrane structure and a liquid polymer-poor phase that formed the membrane pores [38]. The membrane coupons that came off the glass plate were stored in DI water before

characterization and performance evaluation.

2.3 Membrane Characterization

Membrane surface and cross-sectional images were obtained using field emission scanning electron microscopy (FESEM, NOVA NanoSEM 230, FEI Co.). To avoid the deformation during sample preparation, the membrane cross-sections were prepared by fracturing membrane coupons in liquid nitrogen. For SEM imaging, samples were sputtered with gold for 90 s (Headway PWM32-PS-CB15PL). Membrane surface morphology and roughness were also investigated using atomic force microscopy (AFM Veeco NanoMan) in a tapping mode (spring constant of 40 N/ m, resonance frequency of 325 kHz, tip radius of 8 nm, and a cantilever dimension of 125(L) × 30(W) × 4(H) μm). The average surface roughness (Ra, deviation in height) and root-mean-square roughness (Rq, the standard deviation of surface heights) were calculated and given by the instrument software (VEECO Nanoscope). Surface chemistry was studied using Fourier transform infrared spectrometry (FTIR, Nicolette Nexus 470).

Further, membrane surface hydrophilicity was studied by measuring water contact angle using a sessile drop method (Pheonix-300). Before measurement, the membranes were kept in vacuum at 20 °C for 5 h to obtain dry coupons. At least six measurements were conducted for each membrane coupon/case and the average value with standard deviation was obtained and reported.

The gravimetric method was used to estimate the membrane porosity [12]. Membranes were dried in a vacuum oven at room temperature for 24 h and then weighed in an electronic balance to get the dry weight (m_{dry}). The membranes were then immersed in MilliQ water for 24 h and then weighed in wet state after carefully mopping the surface water with clean tissue paper (m_{wet}). The membrane thickness h was measured by an automatic micrometer (Teclock SM-112,

Teclock Corporation), and at least 10 points from three membrane coupons for each case were measured. The average thickness was then obtained. The porosity was calculated as:

$$\varepsilon = \frac{(m_{wet} - m_{dry})/\rho_w}{S \times h} \times 100\% \qquad \text{(Eqn. 1)}$$

where S is the surface area of the cut membrane, h is the thickness of the cut membrane, and ρ_w is density of water, 1,000 kg/m^3.

Membrane mechanical strength was tested and compared (MTS CriterionTM Testing Systems, Model 41). The length of each specimen was set as 5 mm between the clamps, and the width and thickness were previously measured by a microscope (Carl Zeiss). Samples were measured under a 25 N load cell using a constant crosshead rate of 40 mm/s at 50 Hz. The Young's modulus was calculated by the instrument software.

Thermal stability analysis was carried out using thermogravimetric analysis (TGA, TA Q5000). Membrane samples were cut into a small size with weight of 1.8 ± 0.2 mg and placed in small aluminum pan followed by thermal analysis from 25 to 800 °C with a heating rate of 10 °C/min in a nitrogen environment.

2.4 Membrane Permeability and Selectivity

To evaluate the performance of the as-synthesized membranes, the permeability and selectivity tests were performed according to established procedures [39]. The tests were conducted under a direct flow and constant pressure dead-end filtration mode. Solutions (water or 1 g/L bovine serum albumin, Mw ~66 kDa Sigma-Aldrich) were placed in a filtration tank (Millipore Amicon 8200) and pressurized by nitrogen gas at a certain pressure (i.e., 1 bar). The solution was stirred to minimize concentration polarization at the membrane surface. The permeated solution was measured over time using an integrated electronic balance (Mettler Toledo ML1502E) and data was logged automatically at 60 s intervals.

For the rejection test, the membranes were challenged by 1 g/L BSA and 10 mg/L methyl orange (MO) solution. The concentrations of BSA and MO were measured using a UV-vis spectrophotometer (Varian Bio 50) at an absorption peak of 278 and 463 nm, respectively. The solute rejection percentage was calculated using the following equation:

$$\text{Rejection} = \left(1 - \frac{C_p}{C_f}\right) \times 100\% \qquad \text{(Eqn. 2)}$$

Where C_p and C_f are the concentrations of BSA and MO in the permeate and feed solutions, respectively. The rejection rates were averaged to obtain a mean value over a period of filtration time, usually corresponding to the time for filtering 200 mL solution.

2.4 Membrane Fouling and Flux Recovery

For the fouling (resistance) test, pure water was passed through the membrane until the flux remained stable. After that, the solution in the filtration cell was changed into the model protein solution of 1 g/L BSA. The filtration experiment lasted for about 2 h until the flux reached stable. After BSA ultrafiltration, the membrane coupon was taken out from the cell and flushed with MilliQ water for 3 min, mildly sonicated for 1 min in a bath sonicator, and again flushed with MilliQ water for 3 min, on both sides. The membrane coupon was replaced into the cleaned filtration cell, and pure water permeability was re-measured. At least three membrane coupons were tested for each case. The flux recovery ratio (FRR) was calculated using the following equation:

$$FRR = \frac{F_{after}}{F_{before}} \times 100\% \qquad \text{(Eqn. 3)}$$

where F_{before} and F_{after} are the pure water fluxes of the pristine and fouled/cleaned membrane, respectively.

To reveal more fouling details, the total fouling ratio (R_t), reversible fouling ratio (R_r) and irreversible fouling ratio (R_{ir}) were calculated using Eqn 4-6 [40], where F_{BSA} is the flux when

234 filtering 1 g/L BSA solution.

235 $$R_t = \frac{F_{before} - F_{BSA}}{F_{before}}$$ (Eqn. 4)

236 $$R_r = \frac{F_{after} - F_{BSA}}{F_{before}}$$ (Eqn. 5)

237 $$R_{ir} = \frac{F_{before} - F_{after}}{F_{before}}$$ (Eqn. 6)

238

239 # 3. Results and Discussion

240 ## 3.1 Characterization of Graphene Oxides

241 The morphology, size, and surface chemistry of GO and CGO were characterized using
242 TEM, AFM, and XPS, which in part have been previously reported by our group (Figure 2) [36].
243 In terms of morphology, CGO has a distinctive quasi-spherical, crumpled structure, with
244 relatively smooth surfaces and sharp ridges (Figure 2b), which is in contrast to the well-known
245 flat morphology of pristine GO (Figure 2a). Our earlier work revealed that water evaporation
246 during the furnace processing induces a strong caplliary force that effectively crumples flat GO
247 sheets into paper-ball-like structures [26]. We further characterized the particle size distribtuions
248 of GO and CGO using AFM and TEM respectively (Figure 2c). They both have very similar size
249 distributions, and approximately >80% of these particles are between 100 and 400 nm (Figure
250 2c).

251 Surface chemistry of GO and CGO were quantified by XPS. GO is considered as a one-
252 atom-thick planar sp^2-bonded carbon sheet rich in oxygen functional groups (e.g. hydroxyl,
253 epoxy, carbonyl, and carboxyl groups, etc.) [41]. For a furnace temperature of 200 °C, a minor
254 amount of oxygen functional groups were observed to be removed [26]. The high-resolution
255 carbon 1 S peak from XPS spectra was deconvoluted into five oxidation states, which represent

most commonly accounted surface functional components, including the C-C (284.8 eV), C-OH (286.2 eV, 1-1.5 eV shift to higher binding energy (BE)), C-O-C (287.1 eV, higher BE compared to C-OH group), C=O (287.7 eV, 2.5-3 eV shift to higher BE) and COOH (288.8 eV, 4-4.5 eV shift to higher BE) functionalities [42, 43]. As shown in Figure 2d, GO is highly oxidized with abundant oxygen-based functional groups, including C-OH (~13% of area ratio), C-O-C (~ 35%), C=O (~6%), and COOH (~5%). Compared to GO, CGO was only mildly reduced (the C-C area ratios increased from ~41 ± 4 % of GO to ~45 ± 3 % of CGO), and other components remained nearly the same, including C-OH (~8% of area ratio), C-O-C (~ 37%), C=O (~ 5%), and COOH (~5%). The material characterization results show that while the morphology changes, CGO surface chemistry is very similar to GO. This is also consistent with the ζ-potential measurements, with both being around -46 mV (40 mg/L aqueous solution, pH 6.0 ± 0.3).

3.2 Membrane Characterization

The dispersibility of graphene oxides in organic solvents is a critical factor to consider when synthesizing GO-polymer composites including membranes. GO is polar in nature due to oxygen-containing functionalities, therefore polar solvents are thought (and observed) to facilitate its dispersion [44]. A previous study revealed that GO dispersions in organic solvents such as DMF and NMP exhibit long-term stability only when the concentration is lower than 0.5 mg/mL [44]. In this work, sonication was used to exfoliate and disperse GO in NMP. Solid graphene oxide (as a powder, 0, 9, 27 mg) was directly added in the NMP solution (8.1 g) and sonicated for 1 h in order to achieve GO exfoliation and homogeneous mixing (Figure 1). Consistent with the previous study [44], our high GO concentration in NMP (> 1 mg/mL) leads to dispersion of GO flakes, with a few aggregates being observed. In contrast, CGO was observed to disperse well in NMP, even under the highest concentration (3.3 mg/mL). This

observation agrees with our earlier findings of GO/CGO stability in water [36]. GO stability in water significantly increases (by 18-80%) when it is physically crumpled (as CGO), which reduces $\pi-\pi$ interactions between discrete sheets, resulting in enhanced aggregation-resistance.

Casting solutions were used to synthesize membranes via a phase inversion process as described in Section 2.2 and Figure 1. Compared to control PSF membranes that have a white color, membranes incorporated with GO/CGO are gray/black in color (S.I., Figure S1), suggesting successful incorporation of nanomaterials in the polymer matrix. As-synthesized membranes were further characterized by SEM and AFM (Figure 3), and GO or CGO particles were not directly observed on/at the membrane surfaces in top-view SEM images (Figure 3a-e). The direct observation of nanoparticles on the membrane surface depends on the mass percentage (total amount) of nanoparticles blended. For previous reports observing surface nanoparticles, the mass percentage (normalized to the polymer mass) were typically higher than 3% (and up to > 30%) [2, 45, 46]; in contrast, in this work loadings were always lower than 2%. It should be noted that for high aspect ratio materials such as carbon nanotubes, material observation on the surface of similar membranes occurred with mass percentages as low as 1% [12, 47]. Direct comparison of the SEM top-view images show that the membranes became smoother with addition of nanoparticles (Figure 3a-e). The membrane cross-section exhibits a finger-like morphology, typical of PSF UF membranes synthesized via phase inversion (Figure 2f-j). The dense, selective layer forms at the top portion of the membrane structure, and larger pores gradually develop throughout the rest of the membrane. Overall, no significant difference in cross-sectional structure was identified between modified and unmodified membranes. Figure 3(k-o) shows the three-dimensional AFM images of the PSF and composite membrane surfaces. The 3D surface images exhibit the same trends as those directly taken from SEM top-view

images. This was further confirmed by surface roughness properties obtained from AFM analysis, including mean roughness (Ra) and root mean square of Z data (Rq) (Table 1). All the roughness parameters of the composite membranes were smaller than those of the pristine PSF membranes. The average Rq and Ra values for the PSF membrane were 76.2 ± 34.9 and 60.7 ± 29.5 nm, respectively, and for composite membranes, values decreased by ca. 50% (30-45 nm for Rq, and 23-35 nm for Ra, Table 1). Further, surface roughness (Rq) continued to decrease from ~40 nm (with 0.5 wt.% addition) to ~30 nm (with 1.5 wt.% addition), and the variation among measurements also decreased (as indicated by the standard deviation). In other words, with CGO/GO amendment, membranes became relatively smoother. Previously, both increases [12, 46] and decreases [32, 48, 49] in surface roughness have been observed after the incorporation of nanomaterials. It is generally considered that rough surfaces accumulate contaminants in the valleys, leading to increased fouling tendencies [12].

FTIR spectra of PSF and composite membranes do not show significant differences due to the dominance of polysulfone in the composite (S.I., Figure S2). For all, spectra show typical absorption peaks of polysulfone [50]: 1151 cm^{-1} (O-S-O stretching), 1244 cm^{-1} (C-O-C stretching), and 1585 cm^{-1} (C-C aromatic), characteristic of the sulfone group, while absorption peaks 1020 cm^{-1} and 830 cm^{-1} are indicative of C-H stretching of the aromatic ring of polysulfone.

Contact angles (CA), a measurement of surface hydrophilicity, are presented in Table 1. CA values decreased when GO and CGO were added; for control membranes, a CA of 90.6 ± 6.2° was measured, which decreased to below 80° for all composite membranes. In particular, membranes with 0.5% GO addition has a water contact angle of 64.6 ± 4.0°, which is considerably more hydrophilic compared to pristine PSF membrane. Such enhancement is

attributed to the migration of GO particles onto/into the membrane surface during the phase inversion process, thus imparting the surface with hydrophilic oxygen-containing functional groups [12]. Observed CA values also agree well with previous GO composite membranes, which are in the range of 60 - 70° [12, 33, 51].

Based on porosity estimations, studied membranes have porosities ranging from 80 to 85% (Eqn. 1). GO modified membranes have a higher porosity (~ 85%) than those of CGO modified ones (~80-82%) (Table 1). The increase of porosity is due to fast exchange of solvent and non-solvent in the phase inversion process. The addition of hydrophilic particles, under certain concentrations, can increase the thermodynamic instability of the casting system and decrease the de-mixing time of the casting solution. Faster de-mixing leads to more porous and thus more permeable membranes, as described previously by others [10]. However, the addition of (excessive) GO leads to an increase in polymer solution viscosity, resulting in delayed de-mixing and the formation of smaller pores [34, 48, 52]. It is also of note that compared to PSF membranes, CGO-PSF membranes have lower porosity (Table 1).

3.3 Membrane Permeability and Rejection

Figure 4a shows pure water flux of pristine, GO-, and CGO-PSF membranes. Pure water flux through the original PSF membrane was measured to be 60.3 ± 13.8 L/(m^2·h) (LMH). For membranes with 0.5% of GO, permeability increased to 123.2 ± 37.0 LMH (Figure 4a), however for 0.5% CGO loading, the flux decreased to 48.8 ± 3.7 LMH. Further, when the GO and CGO loading further increased to 1.5%, the permeability of pure water decreased to 83.1 ± 19.1 and 30.2 ± 5.1 LMH, respectively. From these results, two take away observations can be made: First, the addition of GO and CGO of the same mass percentage leads to markedly different effects on permeability – GO addition results in an increase of permeability; however, the

addition of CGO has the opposite effect. Second, permeability decreases when the addition of both materials is increased. The increase of flux with addition of GO is consistent with previous studies showing a similar (increasing) trend [14, 30]. This is attributed to a substantial increase in surface/pore hydrophilicity (water CA decreased by about 20°) and relative increase in membrane porosity.

These two observations can be explained by the existence of a tipping mass percentage for nanofiller addition [34, 48, 52, 53]. Overall, the addition of (hydrophilic) nanofillers changes the hydrophilicity and viscosity of the casting solution. Increased hydrophilicity leads to faster exchange of solvent and non-solvent, forming more porous membrane structure; however, with further addition of nanomaterials, the viscosity of the casting solution increases, resulting in less porous structures. Previous studies suggest that a tipping mass percentage is a critical point – after which, the water flux decreases due to the (substantial) increase of casting solution viscosity (i.e. the effect of viscosity increase outweighs that of hydrophilicity increase) [34, 48, 52-54]. The mass percentage can be <1% to a few percent, depending on the additive and polymer types. A decrease in the surface roughness has been observed for suppressed porous structure formation due to slow(er) de-mixing [52].

CGO has a much lower tipping mass percentage value compared to GO. We tested CGO-PSF membranes with 0.25 wt.%, which shows a higher water flux than that of pristine PSF membranes, suggesting a tipping mass percentage value < 0.5%. For GO, the tipping mass percentage value is larger than 0.5%. For comparison, a previous study reported a tipping mass percentage as low as 0.2% for GO materials [53]. This difference is likely due to more effective dispersion/stability of CGO in NMP solvent, thus enhancing its material efficacy (i.e., more interaction surfaces between CGO and PSF molecules). This observation is also supported by the

change in surface hydrophilicity. For casting solutions with higher viscosities, diffusion kinetics are relatively slower for GO/CGO materials. As a result, membranes with 1.5 wt.% addition have decreased surface hydrophilicity compared to those with 0.5 wt.% material addition.

There remains a debate over which factor, pore size (porosity) or hydrophilicity change, is dominant with regard to water permeability enhancement for nano-enabled, ultrafiltration membranes as synthesized by phase inversion. The role of pore size was believed to be more important than surface hydrophilicity as discussed by Razmjou et al.[2] and Li et al.[55]; however, others believe that surface/pore hydrophilicity is key [47, 56]. In this study, CGO-PSF membranes show that while surface hydrophilicity increased, porosity and water permeability decreased. These findings likely suggest that porosity, for these membranes, is the more important variable responsible for changes in water permeability for similar material-based conditions.

Separation performance was evaluated by filtration of BSA and MO solutions (Figure 4b and c). BSA is a serum albumin protein, with a Stokes radius of ca. 3.48 nm for single molecules. With a point of zero charge at pH 5.4, it was found to be negatively charged for our studies (measured by electrophoretic light scattering, pH: ~6.3) [39]. MO is a commonly studied dye, much smaller than BSA with a molecular weight of 327 Da. The rejection rates of BSA are almost the same for all membranes tested – virtually 100% (Figure 4b). For MO, rejection rates were inversely correlated with water flux (Figure 4c); for higher water flux, lower rejection of MO occurred. For example, pristine PSF membranes have a retention rate of 48.9 ± 7.4%. A decrease was observed for GO-PSF membranes with 0.5% material loading (41.4 ± 7.7%) which then increased to 52.7 ± 5.0% for CGO-PSF membrane with 1.5% loading. These results are a classic example of the trade-off between permeability and selectivity.

The membrane rejection mechanisms can include size-, charge-, and adsorption-based mechanisms, among which, size-based (sieving) mechanism is considered to be critical for ultrafiltration membranes. Size exclusion rejection is dependent on the pore size of membranes and molecular weight of the solute. Previous studies have attributed increased protein rejection (with concurrent increase in water permeability) to enhanced adsorption [12, 33], since proteins were observed to have high adsorption tendencies (on/with carbon nanostructures) [57]. Here, we were not able to observe an increase of protein rejection with addition of GO due to the complete rejection of BSA by all membranes evaluated. For the rejection of BSA, we believe it is mainly a size exclusion mechanism, as previous reports of similar membranes revealed a MWCO size of around 50 kDa [58]. Additionally, a hydrophilicity/charge-based mechanism appears to be minimal, as we did not observe higher rejection rates of MO for GO membranes with higher surface hydrophilicity (lower water contact angle).

3.4 Membrane Flux Recovery

Membrane flux recovery data, after fouling and subsequent cleaning, is presented in Figure 5. For pristine PSF membranes, 68.6 ± 25.1% of the water flux could be recovered after BSA fouling and cleaning. However for 0.5% and 1.5% GO-PSF membranes, 52.7 ± 17.0% and 62.8 ± 0.4% of water flux were able to be recovered, respectively. Both were lower than that of pristine PSF membranes. This is in contrast to a number of previous reports that demonstrate modified membranes with higher flux recovery ratio (FRR) compared to pristine ones. For these, enhanced surface hydrophilicity was believed to mitigate protein adsorption due to the repulsion force from the hydrated layers on the surface which also preserves protein (tertiary) structure [33]. However, we did not observe significant FRR enhancement as a function of (enhancement in) surface hydrophilicity. Interestingly, for 0.5% CGO-PSF membranes, the highest water flux

recovery ratio was achieved, with a percentage of 76.3 ± 17.0%. It is also noteworthy that 0.5% CGO-PSF membranes had a lower surface hydrophilicity than 0.5% GO-PSF membranes. These observations suggest that due to relatively larger pore sizes, the GO-PSF membranes had more partially blocked pores during fouling, which subsequently decreased the flux (i.e. size exclusion-based mechanism for solute rejection). This also supports the key role of porosity (pore size), compared to surface hydrophilicity, when determining and predicting membrane performance. Our calculations using Eqn. 4-6 showed that only irreversible fouling existed for these membranes, and the total/irreversible fouling ratios were 0.31, 0.47, 0.24, 0.37, and 0.50 for PSF, 0.5% GO, 0.5% CGO, 1.5% GO, and 1.5% CGO membranes, respectively.

3.5 Mechanical Strength and Thermal Stability

The tensile strength of the membranes are shown in Figure S3. The PSF control membranes have a Young's modulus of 71 ± 8 MPa. With 0.5% addition of GO, the mechanical strength decreased likely due to increased porosity of the membrane; with further increase to 1.5% GO, the strength became similar to that of PSF membranes (69 ± 16 MPa). The low-dimensional carbon nanomaterials were believed to act as extensions for hybrid architectures, which can become entangled with polymer chains, thus enhancing the strength, as noted by others [12]. The eventual strength of the composite membranes was a trade-off between the increase of porosity and the effects of GO as extension. For both CGO scenarios, the strength decreased, which was attributed to the shape effect - the 3D spherical structure likely cannot act similarly for the hybrid architectures compared to 2D structures.

For thermal stability, the PSF and composite membranes did not show difference. They were thermally stable until the temperature reached around 510 °C, agreeing with the reported values in literature [59, 60].

4. Conclusions

In this work, we synthesized, applied, and compared two types of GO material variables, flat GO and crumpled GO (CGO), as nanoscale fillers in polysulfone (PSF) ultrafiltration membranes. Our experimental results show that graphene oxide physical shape leads to varied membrane structures, water flux, and rejection performance(s). These differences are attributed to the (more) effective dispersion of CGO nanoparticles, which considerably lowers the tipping mass percentage for substantial viscosity change of the casting solution. A tipping mass percentage value between < 0.5% is observed for CGO; for GO, the tipping mass percentage value is larger than 0.5%. Results clearly indicate that GO material properties, such as varied shape, affect the dispersion status and subsequent hydrophilicity and viscosity of the mixture casting solutions, thus affecting membrane structure (surface hydrophilicity and porosity) and performance (permeability, rejection, and flux recovery). This study also suggests that a change of porosity is likely to be a more important factor than that of surface hydrophilicity in determining ultrafiltration membrane performance when graphene oxides are applied as nanoscale fillers of these mass percentages.

Acknowledgements

This work was partially supported by National Science Foundation's CAREER Award (CBET 1454656), by the McDonnell Academy Global Energy and Environment Partnership (MAGEEP), Washington University in St. Louis, and the Mindlin Foundation. XPS work was performed at Institute of Materials Science & Engineering, Washington University in St. Louis, with partial support from National Science Foundation under Grant No. CBET 1337374.

References

[1] X. Qu, J. Brame, Q. Li, P.J.J. Alvarez, Nanotechnology for a Safe and Sustainable Water Supply: Enabling Integrated Water Treatment and Reuse, Acc. Chem. Res., 46 (2012) 834-843.
[2] A. Razmjou, J. Mansouri, V. Chen, The effects of mechanical and chemical modification of TiO_2 nanoparticles on the surface chemistry, structure and fouling performance of PES ultrafiltration membranes, J. Membr. Sci., 378 (2011) 73-84.
[3] I.H. Alsohaimi, M. Kumar, M.S. Algamdi, M.A. Khan, K. Nolan, J. Lawler, Antifouling hybrid ultrafiltration membranes with high selectivity fabricated from polysulfone and sulfonic acid functionalized TiO2 nanotubes, Chem. Eng. J., 316 (2017) 573-583.
[4] P. Daraei, S.S. Madaeni, N. Ghaemi, E. Salehi, M.A. Khadivi, R. Moradian, B. Astinchap, Novel polyethersulfone nanocomposite membrane prepared by PANI/Fe3O4 nanoparticles with enhanced performance for Cu(II) removal from water, J. Membr. Sci., 415–416 (2012) 250-259.
[5] J. Yin, E.-S. Kim, J. Yang, B. Deng, Fabrication of a novel thin-film nanocomposite (TFN) membrane containing MCM-41 silica nanoparticles (NPs) for water purification, J. Membr. Sci., 423–424 (2012) 238-246.
[6] B. Díez, N. Roldán, A. Martín, A. Sotto, J.A. Perdigón-Melón, J. Arsuaga, R. Rosal, Fouling and biofouling resistance of metal-doped mesostructured silica/polyethersulfone ultrafiltration membranes, J. Membr. Sci., 526 (2017) 252-263.
[7] K. Zodrow, L. Brunet, S. Mahendra, D. Li, A. Zhang, Q. Li, P.J. Alvarez, Polysulfone ultrafiltration membranes impregnated with silver nanoparticles show improved biofouling resistance and virus removal, Water Res., 43 (2009) 715-723.
[8] L. Huang, S. Zhao, Z. Wang, J. Wu, J. Wang, S. Wang, In situ immobilization of silver nanoparticles for improving permeability, antifouling and anti-bacterial properties of ultrafiltration membrane, J. Membr. Sci., 499 (2016) 269-281.
[9] N. Akar, B. Asar, N. Dizge, I. Koyuncu, Investigation of characterization and biofouling properties of PES membrane containing selenium and copper nanoparticles, J. Membr. Sci., 437 (2013) 216-226.
[10] J.S. Taurozzi, C.A. Crock, V.V. Tarabara, C60-polysulfone nanocomposite membranes: Entropic and enthalpic determinants of C60 aggregation and its effects on membrane properties, Desalination, 269 (2011) 111-119.
[11] C.-F. de Lannoy, D. Jassby, D. Davis, M. Wiesner, A highly electrically conductive polymer–multiwalled carbon nanotube nanocomposite membrane, J. Membr. Sci., 415 (2012) 718-724.
[12] J. Zhang, Z. Xu, W. Mai, C. Min, B. Zhou, M. Shan, Y. Li, C. Yang, Z. Wang, X. Qian, Improved Hydrophilicity, Permeability, Antifouling and Mechanical Performance of PVDF Composite Ultrafiltration Membranes Tailored by Oxidized Low-Dimensional Carbon Nanomaterials, J. Mater. Chem. A, 1 (2013) 3101-3111.
[13] Y. Jiang, P. Biswas, J.D. Fortner, A review of recent developments in graphene-enabled membranes for water treatment, Environ. Sci.: Water Res. Technol., 2 (2016) 915-922.
[14] B.M. Ganesh, A.M. Isloor, A.F. Ismail, Enhanced hydrophilicity and salt rejection study of graphene oxide-polysulfone mixed matrix membrane, Desalination, 313 (2013) 199-207.
[15] J. Yin, G. Zhu, B. Deng, Graphene oxide (GO) enhanced polyamide (PA) thin-film nanocomposite (TFN) membrane for water purification, Desalination, 379 (2016) 93-101.
[16] A. Venault, C.-H. Chiang, H.-Y. Chang, W.-S. Hung, Y. Chang, Graphene oxide/PVDF VIPS membranes for switchable, versatile and gravity-driven separation of oil and water, J. Membr.

Sci., 565 (2018) 131-144.
[17] H. Sun, B. Tang, P. Wu, Hydrophilic hollow zeolitic imidazolate framework-8 modified ultrafiltration membranes with significantly enhanced water separation properties, J. Membr. Sci., 551 (2018) 283-293.
[18] D. Wang, S.E. Gilliland, X. Yi, K. Logan, D.R. Heitger, H.R. Lucas, W.-N. Wang, Iron Mesh-Based Metal Organic Framework Filter for Efficient Arsenic Removal, Environ. Sci. Technol., 52 (2018) 4275-4284.
[19] M. Safarpour, A. Khataee, V. Vatanpour, Thin film nanocomposite reverse osmosis membrane modified by reduced graphene oxide/TiO_2 with improved desalination performance, J. Membr. Sci., 489 (2015) 43–54.
[20] L. Yu, Y. Zhang, B. Zhang, J. Liu, H. Zhang, C. Song, Preparation and characterization of HPEI-GO/PES ultrafiltration membrane with antifouling and antibacterial properties, J. Membr. Sci., 447 (2013) 452-462.
[21] Z. Xu, T. Wu, J. Shi, K. Teng, W. Wang, M. Ma, J. Li, X. Qian, C. Li, J. Fan, Photocatalytic antifouling PVDF ultrafiltration membranes based on synergy of graphene oxide and TiO2 for water treatment, J. Membr. Sci., 520 (2016) 281-293.
[22] J. Yin, B. Deng, Polymer-matrix nanocomposite membranes for water treatment, J. Membr. Sci., 479 (2015) 256-275.
[23] R. Arvidsson, D. Kushnir, B.A. Sandén, S. Molander, Prospective Life Cycle Assessment of Graphene Production by Ultrasonication and Chemical Reduction, Environ. Sci. Technol., 48 (2014) 4529-4536.
[24] W. Cai, R.D. Piner, F.J. Stadermann, S. Park, M.A. Shaibat, Y. Ishii, D. Yang, A. Velamakanni, S.J. An, M. Stoller, J. An, D. Chen, R.S. Ruoff, Synthesis and Solid-State NMR Structural Characterization of 13C-Labeled Graphite Oxide, Science, 321 (2008) 1815-1817.
[25] A. Bagri, C. Mattevi, M. Acik, Y.J. Chabal, M. Chhowalla, V.B. Shenoy, Structural evolution during the reduction of chemically derived graphene oxide, Nat. Chem., 2 (2010) 581-587.
[26] W.-N. Wang, Y. Jiang, P. Biswas, Evaporation-induced crumpling of graphene oxide nanosheets in aerosolized droplets: confinement force relationship, J. Phys. Chem. Lett., 3 (2012) 3228-3233.
[27] Y. Jiang, W.-N. Wang, P. Biswas, J.D. Fortner, Facile aerosol synthesis and characterization of ternary crumpled graphene–TiO_2–magnetite nanocomposites for advanced water treatment, ACS Appl. Mater. Interfaces, 6 (2014) 11766-11774.
[28] W.-N. Wang, Y. Jiang, J.D. Fortner, P. Biswas, Nanostructured graphene-titanium dioxide composites synthesized by a single-step aerosol process for photoreduction of carbon dioxide, Environ. Eng. Sci., 31 (2014) 428-434.
[29] Z. Wang, B. Teychene, T.E. Abbott Chalew, G.S. Ajmani, T. Zhou, H. Huang, X. Wu, Aluminum-humic colloid formation during pre-coagulation for membrane water treatment: Mechanisms and impacts, Water Res., 61 (2014) 171-180.
[30] C.A. Crock, A.R. Rogensues, W. Shan, V.V. Tarabara, Polymer nanocomposites with graphene-based hierarchical fillers as materials for multifunctional water treatment membranes, Water Res., 47 (2013) 3984-3996.
[31] S. Zinadini, A.A. Zinatizadeh, M. Rahimi, V. Vatanpour, H. Zangeneh, Preparation of a novel antifouling mixed matrix PES membrane by embedding graphene oxide nanoplates, J. Membr. Sci., 453 (2014) 292-301.
[32] J. Ma, X. Guo, Y. Ying, D. Liu, C. Zhong, Composite ultrafiltration membrane tailored by

554 MOF@GO with highly improved water purification performance, Chem. Eng. J., 313 (2017)
555 890-898.
556 [33] Z. Xu, J. Zhang, M. Shan, Y. Li, B. Li, J. Niu, B. Zhou, X. Qian, Organosilane-
557 functionalized graphene oxide for enhanced antifouling and mechanical properties of
558 polyvinylidene fluoride ultrafiltration membranes, J. Membr. Sci., 458 (2014) 1-13.
559 [34] S. Ayyaru, Y.-H. Ahn, Application of sulfonic acid group functionalized graphene oxide to
560 improve hydrophilicity, permeability, and antifouling of PVDF nanocomposite ultrafiltration
561 membranes, J. Membr. Sci., 525 (2017) 210-219.
562 [35] M. Li, J. Shi, C. Chen, N. Li, Z. Xu, J. Li, H. Lv, X. Qian, X. Jiao, Optimized permeation
563 and antifouling of PVDF hybrid ultrafiltration membranes: synergistic effect of dispersion and
564 migration for fluorinated graphene oxide, J. Nanopart. Res., 19 (2017) 114.
565 [36] Y. Jiang, R. Raliya, J.D. Fortner, P. Biswas, Graphene oxides in water: correlating
566 morphology and surface chemistry with aggregation behavior, Environ. Sci. Technol., 50 (2016)
567 6964–6973.
568 [37] W.S. Hummers, R.E. Offeman, Preparation of Graphitic Oxide, J. Am. Chem. Soc., 80
569 (1958) 1339-1339.
570 [38] H. Strathmann, K. Kock, The formation mechanism of phase inversion membranes,
571 Desalination, 21 (1977) 241-255.
572 [39] Y. Jiang, W.-N. Wang, D. Liu, Y. Nie, W. Li, J. Wu, F. Zhang, P. Biswas, J.D. Fortner,
573 Engineered crumpled graphene oxide nanocomposite membrane assemblies for advanced water
574 treatment processes, Environ. Sci. Technol., 49 (2015) 6846-6854.
575 [40] M. Kumar, Z. Gholamvand, A. Morrissey, K. Nolan, M. Ulbricht, J. Lawler, Preparation and
576 characterization of low fouling novel hybrid ultrafiltration membranes based on the blends of
577 GO− TiO2 nanocomposite and polysulfone for humic acid removal, J. Membr. Sci., 506 (2016)
578 38-49.
579 [41] K.A. Mkhoyan, A.W. Contryman, J. Silcox, D.A. Stewart, G. Eda, C. Mattevi, S. Miller, M.
580 Chhowalla, Atomic and Electronic Structure of Graphene-Oxide, Nano Lett., 9 (2009) 1058-
581 1063.
582 [42] A. Ganguly, S. Sharma, P. Papakonstantinou, J. Hamilton, Probing the Thermal
583 Deoxygenation of Graphene Oxide Using High-Resolution In Situ X-ray-Based Spectroscopies,
584 J. Phys. Chem. C, 115 (2011) 17009-17019.
585 [43] S. Yumitori, Correlation of C1s chemical state intensities with the O1s intensity in the XPS
586 analysis of anodically oxidized glass-like carbon samples, J. Mater. Sci., 35 (2000) 139-146.
587 [44] J. Paredes, S. Villar-Rodil, A. Martinez-Alonso, J. Tascon, Graphene oxide dispersions in
588 organic solvents, Langmuir, 24 (2008) 10560-10564.
589 [45] V. Vatanpour, S.S. Madaeni, A.R. Khataee, E. Salehi, S. Zinadini, H.A. Monfared, TiO_2
590 embedded mixed matrix PES nanocomposite membranes: Influence of different sizes and types
591 of nanoparticles on antifouling and performance, Desalination, 292 (2012) 19-29.
592 [46] I. Akin, E. Zor, H. Bingol, M. Ersoz, Green Synthesis of Reduced Graphene
593 Oxide/Polyaniline Composite and Its Application for Salt Rejection by Polysulfone-Based
594 Composite Membranes, The Journal of Physical Chemistry B, 118 (2014) 5707-5716.
595 [47] E. Fontananova, V. Grosso, S.A. Aljlil, M.A. Bahattab, D. Vuono, F.P. Nicoletta, E. Curcio,
596 E. Drioli, G. Di Profio, Effect of functional groups on the properties of multiwalled carbon
597 nanotubes/polyvinylidenefluoride composite membranes, J. Membr. Sci., 541 (2017) 198-204.
598 [48] N. Meng, R.C.E. Priestley, Y. Zhang, H. Wang, X. Zhang, The effect of reduction degree of
599 GO nanosheets on microstructure and performance of PVDF/GO hybrid membranes, J. Membr.

Sci., 501 (2016) 169-178.
[49] M. Safarpour, A. Khataee, V. Vatanpour, Preparation of a Novel Polyvinylidene Fluoride (PVDF) Ultrafiltration Membrane Modified with Reduced Graphene Oxide/Titanium Dioxide (TiO2) Nanocomposite with Enhanced Hydrophilicity and Antifouling Properties, Industrial & Engineering Chemistry Research, 53 (2014) 13370-13382.
[50] K. Singh, S. Devi, H.C. Bajaj, P. Ingole, J. Choudhari, H. Bhrambhatt, Optical Resolution of Racemic Mixtures of Amino Acids through Nanofiltration Membrane Process, Sep. Sci. Technol., 49 (2014) 2630-2641.
[51] Z. Wang, H. Yu, J. Xia, F. Zhang, F. Li, Y. Xia, Y. Li, Novel GO-blended PVDF ultrafiltration membranes, Desalination, 299 (2012) 50-54.
[52] H. Sun, B. Tang, P. Wu, Development of Hybrid Ultrafiltration Membranes with Improved Water Separation Properties Using Modified Superhydrophilic Metal–Organic Framework Nanoparticles, ACS Appl. Mater. Interfaces, 9 (2017) 21473-21484.
[53] A. Karkooti, A.Z. Yazdi, P. Chen, M. McGregor, N. Nazemifard, M. Sadrzadeh, Development of advanced nanocomposite membranes using graphene nanoribbons and nanosheets for water treatment, J. Membr. Sci., 560 (2018) 97-107.
[54] S. Xia, M. Ni, Preparation of poly(vinylidene fluoride) membranes with graphene oxide addition for natural organic matter removal, J. Membr. Sci., 473 (2015) 54-62.
[55] J.-F. Li, Z.-L. Xu, H. Yang, L.-Y. Yu, M. Liu, Effect of TiO_2 nanoparticles on the surface morphology and performance of microporous PES membrane, Appl. Surf. Sci., 255 (2009) 4725-4732.
[56] M.-l. Luo, W. Tang, J.-q. Zhao, C.-s. Pu, Hydrophilic modification of poly(ether sulfone) used TiO_2 nanoparticles by a sol–gel process, J. Mater. Process. Technol., 172 (2006) 431-436.
[57] J. Meng, L. Song, H. Xu, H. Kong, C. Wang, X. Guo, S. Xie, Effects of single-walled carbon nanotubes on the functions of plasma proteins and potentials in vascular prostheses, Nanomed. Nanotechnol. Biol. Med., 1 (2005) 136-142.
[58] M.S. Mauter, Y. Wang, K.C. Okemgbo, C.O. Osuji, E.P. Giannelis, M. Elimelech, Antifouling Ultrafiltration Membranes via Post-Fabrication Grafting of Biocidal Nanomaterials, ACS Appl. Mater. Interfaces, 3 (2011) 2861-2868.
[59] X. Lin, S. Kim, D.M. Zhu, E. Shamsaei, T. Xu, X. Fang, H. Wang, Preparation of porous diffusion dialysis membranes by functionalization of polysulfone for acid recovery, J. Membr. Sci., 524 (2017) 557-564.
[60] M.S. Suleman, K.K. Lau, Y.F. Yeong, Enhanced gas separation performance of PSF membrane after modification to PSF/PDMS composite membrane in CO2/CH4 separation, J. Appl. Polym. Sci., 135 (2018) 45650.

639 Figure 1. Schematic diagram of GO- and CGO-PSF membrane fabrication.

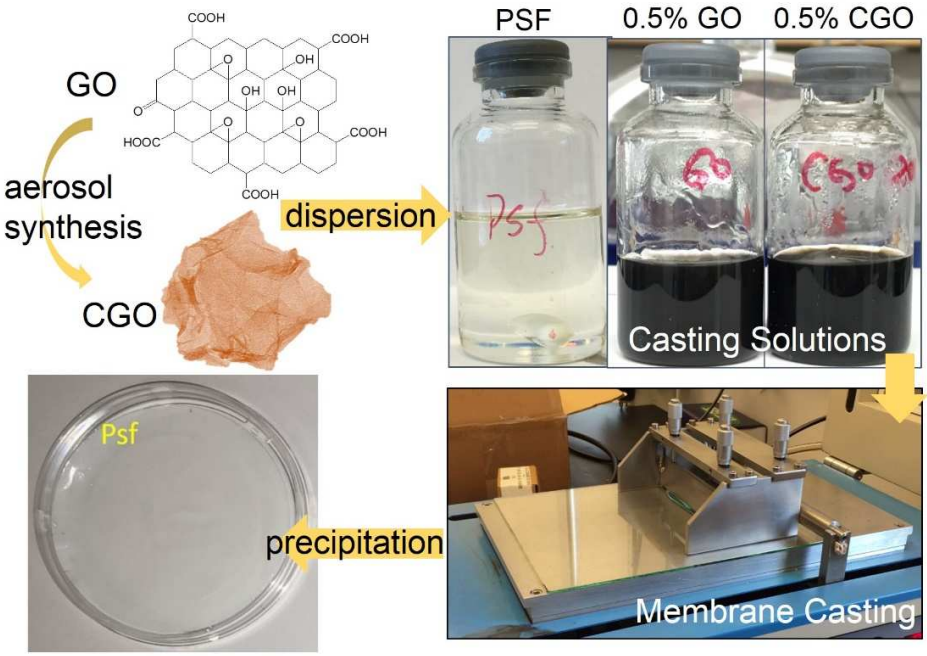

640
641
642
643
644
645
646
647
648
649
650
651
652
653
654
655
656

Figure 2. Material characterization of GO and CGO: (a) and (b), TEM images of GO and CGO; (c) size distribution of GO and CGO obtained by analyzing AFM and TEM images respectively; (d) surface chemistry information obtained by analyzing XPS data.

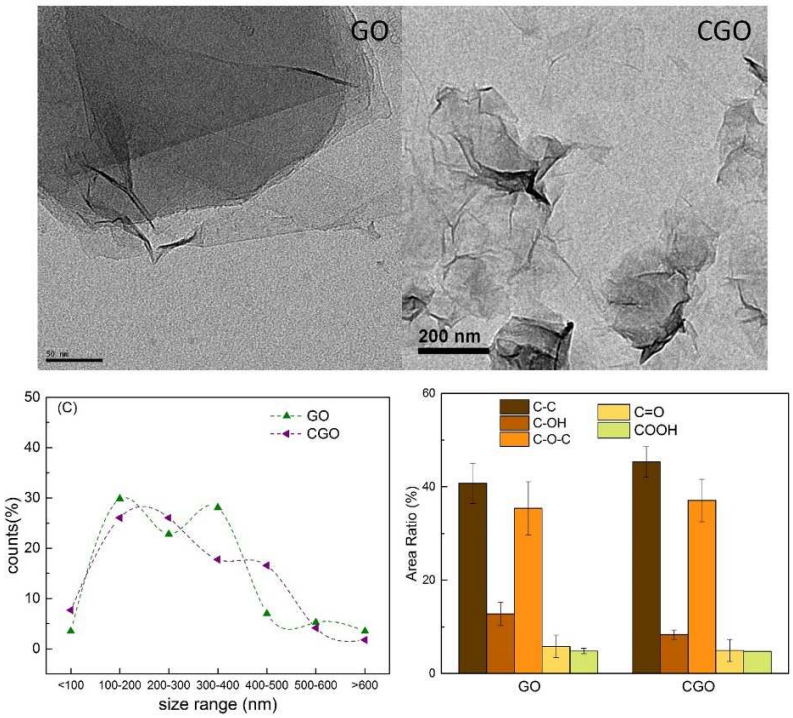

Figure 3. Top view (a-e) and cross-section view (f-j) SEM, AFM (k-o) of PSF, and GO, CGO-PSF membranes (with 0.5% and 1.5% material loading).

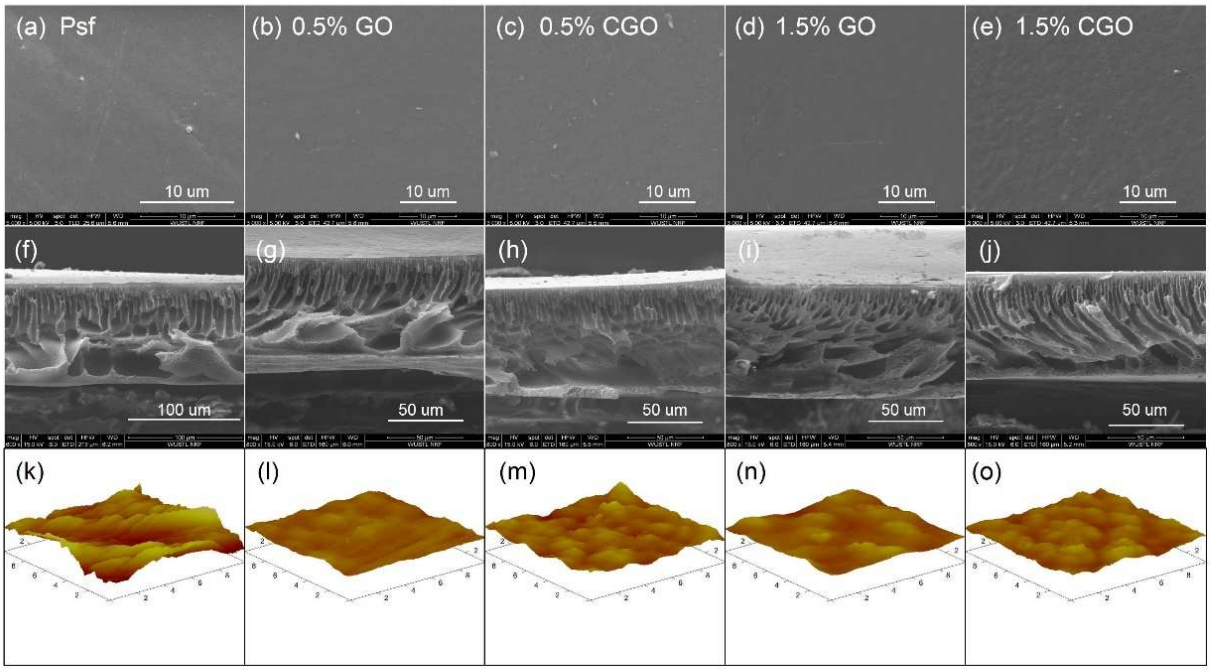

693 Figure 4. Pure water permeability and rejection performances of the pristine PSF and GO/CGO-
694 PSF membranes.

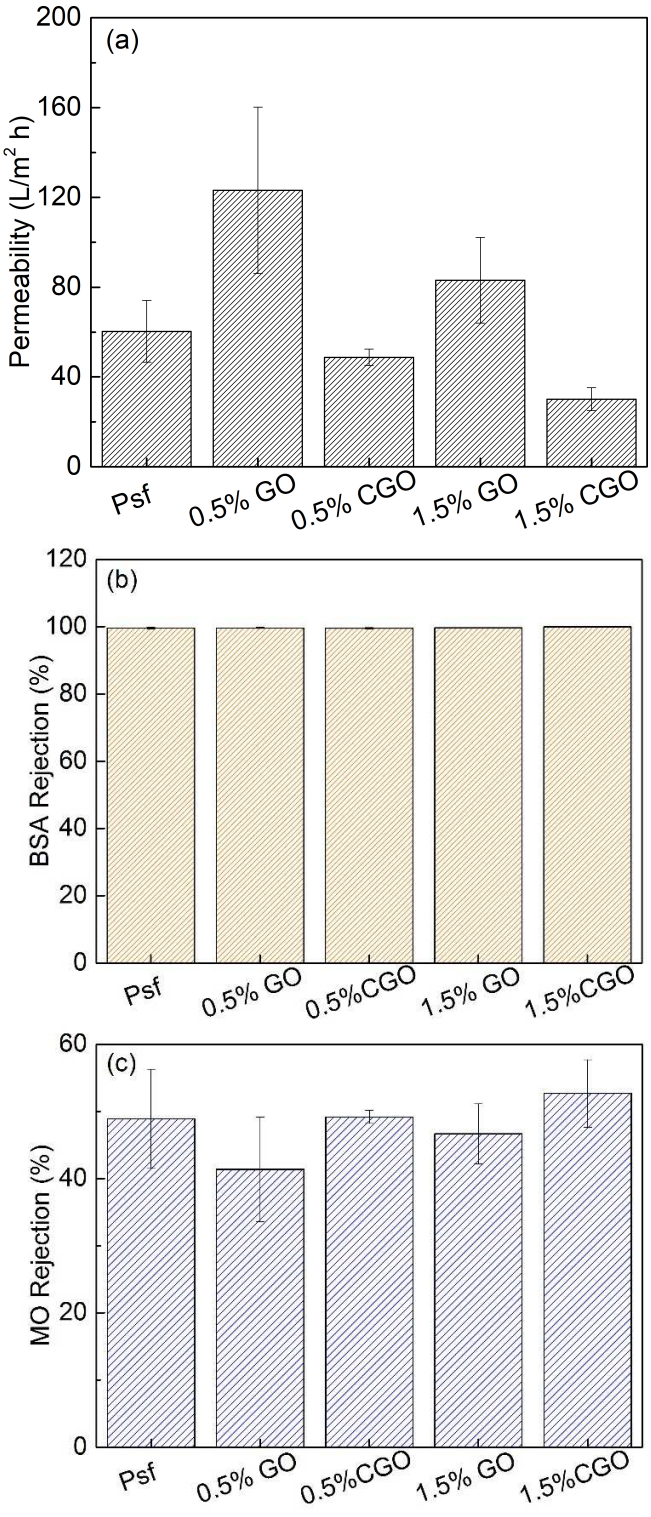

695

696

697

698

699 Figure 5. Recovery of membrane flux after BSA fouling

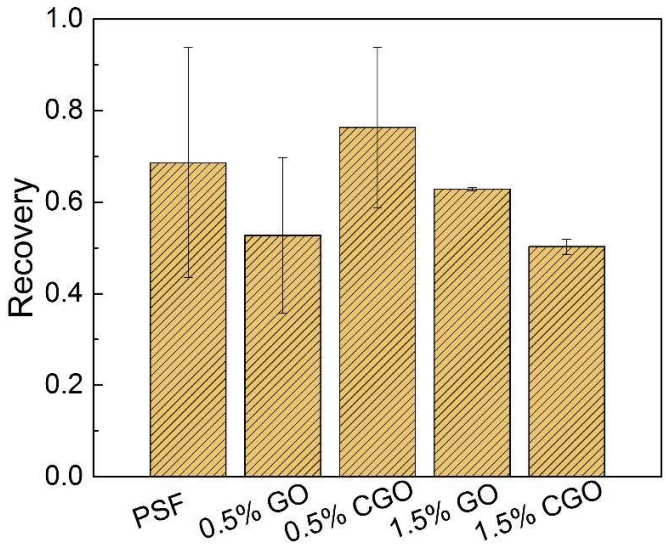

700
701
702
703
704
705
706
707
708
709
710
711
712
713
714
715
716

717 Table 1. Porosity and surface roughness of PSF and GO, CGO-PSF composite membranes.

718

Membranes	Water CA (°)	Porosity	Rq (nm)	Ra (nm)	Rmax (nm)
PSF	90.6 ± 6.2	83.8 ± 4.6%	76.2 ± 34.9	60.7 ± 29.5	553.6 ± 235.7
0.5% GO	64.6 ± 4.0	84.7 ± 5.0%	37.5 ± 30.8	27.9 ± 20.7	303.3 ± 263.0
0.5% CGO	76.4 ± 6.1	82.6 ± 8.9%	45.0 ± 22.7	34.7 ± 16.1	316.3 ± 141.5
1.5% GO	73.1 ± 3.4	85.1 ± 14.0%	31.6 ± 4.3	23.1 ± 3.9	277.3 ± 43.0
1.5% CGO	78.3 ± 8.9	80.0 ± 7.7%	30.8 ± 1.2	24.5 ± 1.3	211.0 ± 23.4

719

720

721

722

Hi Nandhini,

Please see attached. Let me know if you need anything else from me!

Best,

John

John D. Fortner
Associate Professor
International Center for Energy, Environment and Sustainability
Department of Energy, Environmental and Chemical Engineering
Washington University in St. Louis

Office: 314-935-9293
jfortner@wustl.edu

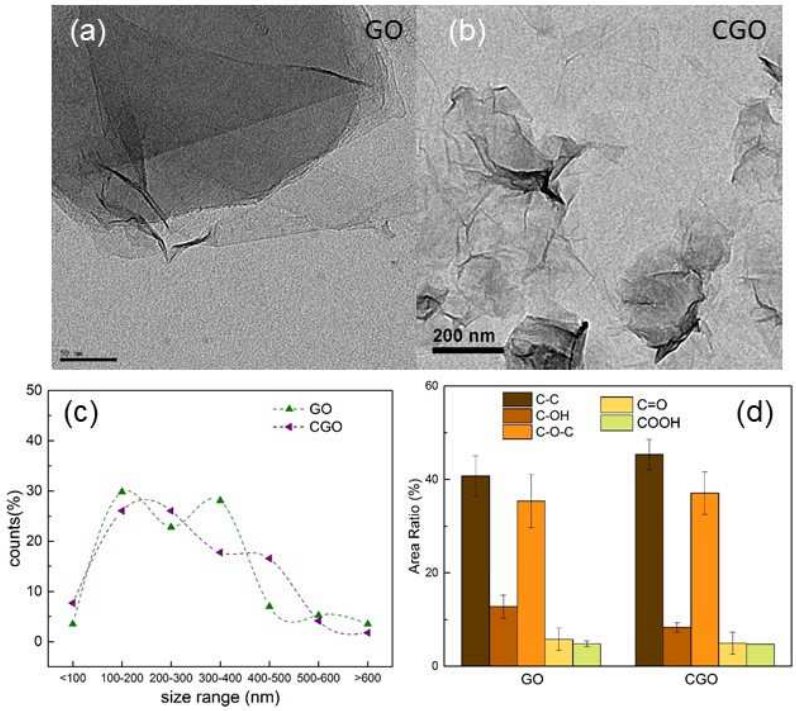

Highlights

- Graphene oxide materials of different shapes led to varied membrane structure and performance.
- More effective dispersion/stability of crumpled graphene oxide nanoparticles in NMP considerably lowers the tipping mass percentage value for viscosity change of the casting solution.
- Change(s) in porosity is likely to be a more important factor than that of surface hydrophilicity in determining UF membrane performance when graphene oxides are applied with these mass percentages.